Nonlinear Optimal Stabilising Control of a Two-wheel Robot

KOKKRATHOKE, Surapong, RAWSTHORNE, Andy, ZHANG, Hongwei <http://orcid.org/0000-0002-7718-021X> and XU, Xu <http://orcid.org/0000-0002-9721-9054>

Nonlinear Optimal Stabilising Control of a Two-wheel Robot

Surapong Kokkrathoke, Andy Rawsthorne, Hongwei Zhang and Xu Xu*

Materials and Engineering Research Institute & Department of Engineering and Mathematics,
College of Business, Technology and Engineering,
Sheffield Hallam University,
Sheffield, UK. S1 1WB
Email: surapong.kokkrathoke@student.shu.ac.uk
Email: a.rawsthorne@shu.ac.uk
Email: h.zhang@shu.ac.uk
*Email: xu.xu@shu.ac.uk
*Corresponding author

Abstract: The stabilisation of a two-wheel robot is a classical benchmarking problem for determining the effectiveness of a control technique. In this paper, a nonlinear optimal control technique is applied to a two-wheel robot which demonstrates excellent control performance comparing against the linear quadratic regulator technique. Simulation results demonstrated that this nonlinear optimal controller can achieve accurate tracking of wheel angular displacement and effective stabilisation of the robot from a very large range of initial pitch angles. Practical factors such as maximum motor voltages are considered and analysed using an extended state-space model to embed such control saturations. Significantly, the two-wheel robot can be balanced from a body pitch angle of up to 88.0° with a maximum motor voltage of 48V using the proposed nonlinear optimal control technique, larger than any other methods achieved in the literature. Controllability studies are also performed throughout this research to facilitate understanding and visualisation of the substantial stabilisation ranges with and without control saturations.

Keywords: nonlinear system; optimal stabilising control; controllability; two-wheel robot.

Reference to this paper should be made as follows: Kokkrathoke, S., Rawsthorne, A., Zhang, H. and Xu, X. (2020) 'Nonlinear Optimal Stabilising Control of a Two-wheel Robot', *Int. J. Modelling, Identification and Control*, Vol. X, No. X, pp.000–000.

Biographical notes: Surapong Kokkrathoke received his MSc in Automation Control and Robotics from Sheffield Hallam University, United Kingdom. He worked as an Electrical Engineer at Synchrotron Light Research Institute (SLRI) in Thailand. Recently, he is PhD scholar student in Sheffield Hallam University sponsored by The SLRI and the Royal Thai Government in the Automation Control and Robotics area.

Andy Rawsthorne received his BEng in Electrical and Electronic Engineering from the University of Manchester Institute of Science and Technology and his MSc in Automation and Robotics from the University of Salford. He worked as researcher in Advanced Robotics at the University of Salford followed by a period working in industry in the areas of industrial automation and robotics. In 2011 he joined Sheffield Hallam University as a Lecturer. Currently he is a Principal Lecturer in Automation and Robotics and Subject Group Leader of the Power, Electrical and Control Engineering subject area. His current research interests include industrial robotics, bipedal locomotion, non-linear control, underactuated systems and industrial automation.

Hongwei Zhang obtained his BEng degree in Automatic Control, MSc in Control Engineering and PhD in Aerospace Engineering all from Harbin Institute of Technology, China. Hongwei has also completed a PhD in Control Engineering at The University of Manchester in the UK. Hongwei is currently working as the interim Head of the Department at the Department of the Engineering and Mathematics at Sheffield Hallam University in the UK. His research interests are in the field of advanced control and condition monitoring of complex processes, industrial automation and robotics, and applications of artificial intelligence.

Xu Xu obtained her BEng degree in Automation from Xidian University, China, an MSc in Control Systems Engineering (with Distinction) and a PhD in nonlinear systems and cellular maps, both in the University of Sheffield (UoS), UK. She worked as a Postdoctoral Researcher at UoS, followed by the positions of Lecturer, Senior Lecturer and now Reader at Sheffield Hallam University, UK.

Her current research interests include nonlinear control techniques and related control engineering applications, cellular automata, swarm robotics, and multi-component lattice Boltzmann fluid dynamics simulation methods and their applications.

1 Introduction

An underactuated system is one in which there are fewer control inputs than degrees of freedom. Underactuated systems are apparent in many applications, for example, underwater, space, flying, mobile robots and flexible robots. An inherent property of these systems is that they contain non-linearities and are often highly unstable. Typical examples include the Acrobot (Spong, 1995), Pendubot (Spong and Block, 1995), Passive Walker (McGeer, 1990), Quadrotor UAV (Jasim and Gu 2018, Nadda and Swarup 2020), Inverted Pendulum (Boubaker, 2013) and Double Inverted Pendulum (Elkinany et. al. 2020).

The inverted pendulum is a widely studied problem in control theory and a useful test bed for experimentation on underactuated systems. A typical approach to the problem of controlling the inverted pendulum is to linearise around an operating point (ordinarily 0 degrees) by means of a Taylor series expansion (Boubaker, 2013). When the pendulum approaches this operating point, standard methods of linear control can be applied, for example PID (Shalaby, El-Hossainy and Abo-Zalam, 2019) or linear quadratic regulator (LQR) (Maity and Luecke, 2019). Whilst this approach enables control within a small bounded range of angles, multiple control strategies need to be applied with this approach; the first to swing the pendulum close to the controlled point, and the second to control the pendulum angle around this operating point. Other more recent control methods applied to the inverted pendulum, including backstepping (Huang et. al., 2019a), high-order disturbance observer based sliding mode control (Huang et. al, 2019b) and perceptual control (Johnson et. al., 2020), all share the same foundation.

Xu, Zhang and Carbone (2017) applied a global non-linear control method known as Nonlinear Freezing Optimal Control (NFOC) in order to accurately and efficiently control the pendulum from any given initial starting angle.

NFOC is a global nonlinear control technique that can be applied to any general nonlinear system and can be optimised against a specific cost function (Banks and Mhana, 1992; McCaffrey and Banks, 2001). Further details regarding the derivation of this method and application can be found in section 3 of this paper.

An expansion of the principle of the inverted pendulum is that of the wheeled inverted pendulum. The wheeled inverted pendulum possesses both interest from a theoretical perspective but also from a practical perspective for use of a wheeled mobile robot. Two-Wheel Robots (TWR) possess good manoeuvrability, an ability to locomote over a wide range of different terrains and ability to turn on a small radius. There have been numerous studies devoted to these devices, for example, in (Grasser et al., 2002) and (Salerno and Angeles, 2003), and use of the mechanism within personal transportation devices (Segway, 2020). Just as with the inverted pendulum, these devices are non-linear and underactuated.

A number of studies have been undertaken on wheeled inverted pendulum and their control systems, a common approach being similar to that of the inverted pendulum with the linearisation of the systems around a vertical operating point (Ren, Chen and Chen, 2008). There are some notable alternative approaches: (i). Kim, Kim and Kwak (2006) presented a wheeled inverted pendulum robot and analysed its performance when progressing over an inclined surface; (ii). Pathak, Franch and Agrawal (2005) applied the principle of partial feedback linearisation which is a familiar approach to the control of underactuated robots (Spong, 1995); (iii). Huang et al. (2010) presented a sliding mode controller approach which was able to tolerate both parameter uncertainty and external disturbances although in performance could only control to within the bounds of a linearised system. It is worth noting that the performance when controlling the pitch angle of these systems is similar in range to the linearised approach; (iv). Guo, Rizvi and Lin, 2021) developed a feedback-based reinforcement learning algorithm which produced converged LQR solution, without the knowledge of system parameters, to control a self-balancing TWR .

Rigatos et al. (2020) proposed a nonlinear optimal control method which linearised around temporary operating point at each time step using a Taylor expansion and Jacobian matrix, an H-infinity feedback controller was developed taking into account the disturbance effect. It is worth noting that the majority of disturbance was due to Taylor series truncation performed to linearise around the temporary operating point. Unlike this paper and the preceding studies, control of the pitch angle was not simulated.

It will be shown in this paper that by application of a Nonlinear Freezing Optimal Controller to a Two-wheel Robot, it provides significant advantages over other approaches. Firstly, the method proposed is a global control strategy which is able to stabilise a much

larger range of robot pitch angles than what were shown in others based on linear techniques. For example, (Guo, Rizvi and Lin, 2021) and (Maity and Luecke, 2019) both used LQR based control approaches and demonstrated narrow balancing ranges of up to 0.1 rad (~5.7°) and 4.5°, respectively. Secondly, the NFOC method can control all (multiple) state variables simultaneously; in addition to robot pitch angle, pitch angular velocity, wheel angular displacement, and wheel angular velocity can also be controlled. This is more efficient over traditional single input single output control methods, where multiple controllers are required, for example, to control pendulum angle and cart position (Shalaby, El-Hossainy and Abo-Zalam, 2019). The NFOC method proposed is robust and due to the recalculation of control gains at every iteration step, disturbance effects are minimised. Finally, this method is an extension of optimal control so can calculate control gains flexibly with an optimised cost function which is able to minimise control energy consumption.

The structure of this paper is as follows: in Section 2, nonlinear dynamic models of the prototype two-wheel robot is developed, using forces and then motor voltages as control inputs. In Section 3, the background and theory of NFOC are explained and a NFOC controller is designed for the two-wheel robot. The simulation results are presented, together with analysis and detailed discussion in Section 4. Finally, in Section 5, concluding remarks are presented.

2 Dynamic Model of the Two-Wheel Robot

2.1. Two-Wheel Robot prototype using Lego EV3

A TWR shares many similarities with and can be modelled in a similar manner as a two-wheel inverted pendulum and cart system (Xu, Zhang and Carbone, 2017; Rigatos et al. 2020). Figure 1 shows a two-wheel robot constructed using Lego EV3 components from a side view and a top view. The angels indicated in Figure 1 are: θ, average wheel angular displacement between the left and right wheels; ψ, pitch angle of the robot body; and ϕ, yaw angle of the robot body, all in radians.

2.2. Nonlinear Model with Control Forces

The dynamical model of the TWR can be obtained using a variety of methods, such as using force analysis and the Newton's law, the Hamiltonian equation and the Lagrangian method. Here, the Lagrangian approach is adopted, such that the Lagrangian equation is calculated as follows:

$$L = T - V, \tag{1}$$

$$\frac{d}{dt}\frac{\partial L}{\partial \dot{x}_j} - \frac{\partial L}{\partial x_j} = \mathrm{F}_j\,, \qquad 1 \le j \le n, \tag{2}$$

where L, T, V, x_j and F_j represent the Lagrangian expression, generalised kinetic energy, generalised potential energy, the *jth* generalised coordinate of the nth dimensional system, and the *jth* generalised force applied on the object, respectively.

The kinetic energy of the TWR system, T (the sum of translational energy T_1 and rotational energy T_2) and the potential energy V can be calculated as shown in (Yamamoto, 2009) as follows:

$$T_1 = \frac{1}{2}m\left[2R^2\dot{\theta}^2 + \frac{W^2}{2}\dot{\phi}^2\right] + \frac{1}{2}M\left[R^2\dot{\theta}^2 + L^2 sin^2\psi\,\dot{\phi}^2 + 2RL\dot{\theta}cos\,\psi\,\dot{\psi} + L\dot{\psi}^2\right],$$

$$T_2 = \frac{1}{2}J_w\left(2\dot{\theta}^2 - \frac{W^2\dot{\phi}^2}{2R^2}\right) + \frac{1}{2}J_\psi\dot{\psi}^2 + \frac{1}{2}J_\phi\dot{\phi}^2 + \frac{1}{2}n^2J_m\left[2\dot{\theta}^2 + 2\dot{\psi}^2 - 4\dot{\theta}\dot{\psi} + \frac{W^2\dot{\phi}^2}{2R^2}\right],$$

and

$$V = 2mgR + MgR + MgLcos\,\psi,$$

where m, M, R, W, L, J_w, J_ψ, J_ϕ, J_m and g denote the wheel mass, the robot body mass, the wheel radius, the robot body width, the distance between the wheel axle and the robot's centre of mass, the wheel's inertia moment, the robot body's pitch inertia moment, the robot body's yaw inertia moment, the DC motor's inertia moment and acceleration due to gravity, respectively. $\dot{\theta}$, $\dot{\psi}$ and $\dot{\phi}$ represent the average wheel angular velocity, the robot body pitch angular velocity and the robot body yaw angular velocity, respectively.

Substitute the energy expressions into Eq.s (1-2), a nonlinear dynamic model of the TWR system can be obtained similarly as obtained in (Yamamoto, 2009). In order to demonstrate the effectiveness of the NFOC technique utilised in this paper and for the ease of understanding, the TWR's motion is restricted to be within a two-dimensional plane and the robot's yaw movement is not considered. To achieve a simpler dynamic model, the robot's yaw angle ϕ is neglected and the focus are on: (i). the regulation of the most unstable (and therefore most challenging) variable - the robot's pitch angle ψ and (ii). the tracking of the wheels' angular displacement θ. This approach proves to be computationally efficient, as the dimensions of the TWR's state-space model reduce to 4 for a regulator design and to 5 for a single reference tracking control design. As introduced in Section 1, the NFOC method applies to any general nonlinear control system (Banks and Mhana, 1992) and (McCaffrey and Banks, 2001), therefore, the optimal control of the TWR system's full set of state-space variables is entirely achievable, using more powerful computing resources.

Now simplifying the TWR's dynamic model by neglecting the yaw motion and organising the nonlinear

model into a state-space matrix form, the following is obtained:

$$\begin{pmatrix}\dot{x}_1\\ \dot{x}_2\\ \dot{x}_3\\ \dot{x}_4\end{pmatrix}=\begin{pmatrix}0 & 1 & 0 & 0\\ 0 & 0 & \frac{e_{23}(x_3)}{[a+b(x_3)]x_3} & \frac{e_{24}(x_3,x_4)}{a+b(x_3)}\\ 0 & 0 & 0 & 1\\ 0 & 0 & \frac{e_{43}(x_3)}{[a+b(x_3)]x_3} & \frac{e_{44}(x_3,x_4)}{a+b(x_3)}\end{pmatrix}\begin{pmatrix}x_1\\ x_2\\ x_3\\ x_4\end{pmatrix}$$
$$+\begin{pmatrix}0 & 0\\ \frac{f_{21}}{a+b(x_3)} & \frac{f_{22}(x_3)}{a+b(x_3)}\\ 0 & 0\\ \frac{f_{41}(x_3)}{a+b(x_3)} & \frac{f_{42}}{a+b(x_3)}\end{pmatrix}\begin{pmatrix}F_\theta\\ F_\psi\end{pmatrix}$$

where $x_1=\theta, x_2=\dot{\theta}, x_3=\psi, x_4=\dot{\psi}$, the functions are defined as:

$b(x_3)=M^2R^2L^2\,sin(x_3)^2+4MLRcos(x_3)n^2J_m,$

$e_{23}(x_3)=2n^2J_mMgLsin(x_3)$
$-M^2RL^2cos(x_3)g\,sin(x_3),$

$e_{24}(x_3,x_4)=x_4\sin(x_3)(M^2RL^3+2MRLn^2J_m$
$+MRLJ_\psi),$

$e_{43}(x_3)=MgLsin(x_3)(2n^2J_m+2J_w+2mR^2$
$+MR^2),$

$e_{44}(x_3,x_4)=x_4\sin(x_3)(-M^2R^2L^2cos(x_3)$
$+2MRLn^2J_m),$

$f_{22}(x_3)=f_{41}(x_3)=2n^2J_m-MRLcos(x_3),$

and the parameters are defined as:

$a=2J_wJ_\psi+2mR^2ML^2+4mR^2n^2J_m+2MR^2n^2J_m$
$+2n^2J_mML^2+2mR^2J_\psi+MR^2J_\psi+2J_wML^2$
$+4J_wn^2J_m+2n^2J_mJ_\psi,$

$f_{21}=ML^2+2n^2J_m+J_\psi,$

$f_{42}=2n^2J_m+2J_w+2mR^2+MR^2,$

Note, the state-space representation of any dynamic system is non-unique and the choice of a particular state-space model affects the controllability of the system. This point will be discussed in more detail in Section 4.1.

2.3. Nonlinear Tracking Model with Control Voltages

In Section 2.2, the dynamics and a nonlinear state-space model of the TWR were presented, using generalised forces F_θ and F_ψ as control inputs. In reality, these forces in a TWR robot system are generated by motors. For example, in the Lego EV3 TWR robot introduced in Section 2.1, two DC motors (left and right) are used to generate such forces and the relationship between the forces and the motor voltages can be found by following Yamamoto's work (2009) as shown below:

$F_\theta=c(v_1+v_2)-2(d+f_w)x_2+2dx_4,$

$F_\psi=-c(v_1+v_2)+2d(x_2-x_4),$

where v_1 and v_2 represent the left and right DC motor voltages which are the new control signals, f_w represents the friction coefficient between the wheel and the ground surface, and parameters $c=\frac{nK_t}{R_m}$ and $d=\frac{nK_tK_b}{R_m}+f_m$, with n, K_t, K_b, R_m and f_m denoting the gear ratio, the DC motor torque constant, the DC motor back EMF constant, the DC motor resistance and the friction coefficient between the robot body and the DC motor, respectively.

Next, a new variable x_5 is introduced as:

$$\dot{x}_5=x_1$$

to assist the design of a nonlinear optimal tracking system which can follow a pre-defined wheel angular displacement reference, in Section 3.2. A new nonlinear state-space model of the TWR for tracking the wheel angle, with DC motor voltages as control inputs, can therefore be written as the following:

$e_{m22}(x_3)=2df_{22}(x_3)-2(d+f_w)f_{21},$

$e_{m24}(x_3,x_4)=e_{24}(x_3,x_4)+2d[f_{21}-f_{22}(x_3)],$

$$\begin{pmatrix}\dot{x}_1\\ \dot{x}_2\\ \dot{x}_3\\ \dot{x}_4\\ \dot{x}_5\end{pmatrix}=\begin{pmatrix}0 & 1 & 0 & 0\\ 0 & \frac{e_{m22}(x_3)}{a+b(x_3)} & \frac{e_{23}(x_3)}{[a+b(x_3)]x_3} & \frac{e_{m24}(x_3,x_4)}{a+b(x_3)}\\ 0 & 0 & 0 & 1\\ 0 & \frac{e_{m42}(x_3)}{a+b(x_3)} & \frac{e_{43}(x_3)}{[a+b(x_3)]x_3} & \frac{e_{m44}(x_3,x_4)}{a+b(x_3)}\\ 1 & 0 & 0 & 0\end{pmatrix}$$
$$\times\begin{pmatrix}x_1\\ x_2\\ x_3\\ x_4\\ x_5\end{pmatrix}+\begin{pmatrix}0 & 0\\ \frac{f_{m21}(x_3)}{a+b(x_3)} & \frac{f_{m22}(x_3)}{a+b(x_3)}\\ 0 & 0\\ \frac{f_{m41}(x_3)}{a+b(x_3)} & \frac{f_{m42}(x_3)}{a+b(x_3)}\\ 0 & 0\end{pmatrix}\begin{pmatrix}v_1\\ v_2\end{pmatrix},\quad(3)$$

where new functions are defined based on the function in Section 2.2 as follows:

$e_{m22}(x_3)=2df_{22}(x_3)-2(d+f_w)f_{21},$

$e_{m24}(x_3,x_4)=e_{24}(x_3,x_4)+2d[f_{21}-f_{22}(x_3)],$

$f_{m21}(x_3)=f_{m22}(x_3)=c[f_{21}-f_{22}(x_3)],$

$e_{m42}(x_3)=2df_{42}-2(d+f_w)f_{41}(x_3),$

$e_{m44}(x_3,x_4)=e_{44}(x_3,x_4)+2d[f_{41}(x_3)-f_{42}],$

$f_{m41}(x_3)=f_{m42}(x_3)=c[f_{41}(x_3)-f_{42}].$

2.4. Linearisation

The proposed optimal stabilising controller design in Section 3 utilises a NFOC technique and will have the capability of controlling the TWR system globally. Traditionally, TWR (and more generally, the inverted pendulum (Rigatos et al. 2020; Boubaker 2013) system are linearised around the top equilibrium using Taylor series expansion. In order to be able to compare stabilising control results between the nonlinear freezing technique adopted with the conventional linear ones in Section 4.2, here, linearisation in a small neighbourhood of the top equilibrium (around when the TWR is in the upright position and has a very small pitch angular velocity) is performed, assuming:

$sin(x_3) \approx x_3,\ cos(x_3) \approx 1, sin\ (x_3)^2 \approx 0$ and $x_4\ sin(x_3) \approx 0$.

Then an approximated linear model is obtained as follows:

$$\begin{pmatrix} \dot{x}_1 \\ \dot{x}_2 \\ \dot{x}_3 \\ \dot{x}_4 \\ \dot{x}_5 \end{pmatrix} = \begin{pmatrix} 0 & 1 & 0 & 0 \\ 0 & \frac{e_{m22L}}{a+b_L} & \frac{e_{23L}}{a+b_L} & \frac{e_{m24L}}{a+b_L} \\ 0 & 0 & 0 & 1 \\ 0 & \frac{e_{m42L}}{a+b_L} & \frac{e_{43L}}{a+b_L} & \frac{e_{m44L}}{a+b_L} \\ 1 & 0 & 0 & 0 \end{pmatrix} \begin{pmatrix} x_1 \\ x_2 \\ x_3 \\ x_4 \\ x_5 \end{pmatrix} + \begin{pmatrix} 0 & 0 \\ \frac{f_{m21L}}{a+b_L} & \frac{f_{m22L}}{a+b_L} \\ 0 & 0 \\ \frac{f_{m41L}}{a+b_L} & \frac{f_{m42L}}{a+b_L} \\ 0 & 0 \end{pmatrix} \begin{pmatrix} v_1 \\ v_2 \end{pmatrix}, \quad (4)$$

where constants are defined as below:

$e_{m22L} = 2df_{22L} - 2(d + f_w)f_{21}$,
$f_{22L} = f_{41L} = 2n^2J_m - MRL$,
$b_L = 4MLRn^2J_m$,
$e_{23L} = 2n^2J_mLMg - M^2RL^2g$,
$e_{m24L} = 2d(f_{21} - f_{22L})$,
$e_{m42L} = 2df_{42} - 2(d + f_w)f_{41L}$,
$e_{43L} = MgL(2n^2J_m + 2J_w + 2mR^2 + MR^2)$,
$e_{m44L} = 2d(f_{41L} - f_{42})$,
$f_{m21L} = f_{m22L} = c(f_{21} - f_{22L})$,
$f_{m41L} = f_{m42L} = c(f_{41L} - f_{42})$.

3 Nonlinear Optimal Controller Design

3.1 Linear Quadratic Regulating and Tracking Method

Linear control systems in general can be represented in the form of:

$$\dot{\boldsymbol{x}} = \boldsymbol{Ax} + \boldsymbol{Bu}\ , \quad (5)$$

where $\boldsymbol{x}$ and $\boldsymbol{u}$ denote the state variable vector and the control vector, and $\boldsymbol{A}$ and $\boldsymbol{B}$ are the system matrix and the control matrix. Note, to design any state-space controllers such as the LQR, matrices $\boldsymbol{A}$ and $\boldsymbol{B}$ must satisfy the controllability or at least the stabilisability requirement.

In a linear quadratic regulating or tracking system, a quadratic infinite-time cost function can be defined as follows (Ogata, 2002):

$$J = \frac{1}{2}\int_0^\infty \left(\boldsymbol{x^T Q x} + \boldsymbol{u^T R u}\right) dt$$

which generates a local optimal feedback control solution given by:

$$\boldsymbol{u} = -\boldsymbol{Kx} = -\boldsymbol{R^{-1}B^T P x}\ , \quad (6)$$

where $\boldsymbol{Q}$, $\boldsymbol{R}$ and $\boldsymbol{P}$ are all positive-definite Hermitian or real symmetric matrices. In particular, $\boldsymbol{Q}$ and $\boldsymbol{R}$ are weighting matrices which jointly determine the relative importance between reducing errors and reducing control energy expenditure. Matrix $\boldsymbol{P}$ is the solution of the algebraic Riccati equation in the form of:

$$\boldsymbol{A^T P + PA + Q - PBR^{-1}B^T P = 0}\ .$$

Substituting Eq. (6) into Eq. (5), the implementable stable controlled system is represented by:

$$\dot{\boldsymbol{x}} = \left(\boldsymbol{A - BR^{-1}B^T P}\right)\boldsymbol{x},$$

with the condition that $\left(\boldsymbol{Q^{\frac{1}{2}}, A}\right)$ is an observable pair.

This linear optimal control technique can be applied to the linearised model of the TWR presented in Section 2.4 to track wheel angle reference and regulate all other variables. Simulation results will be shown and discussed in comparison with the results from the nonlinear control method in Section 4.

3.2 Nonlinear Optimal Control Strategy

Dynamical models of most nonlinear systems can be constructed in the following state-space form (Xu, Zhang and Carbone, 2017):

$$\dot{\boldsymbol{x}} = \boldsymbol{f}(\boldsymbol{x}, \boldsymbol{u}) = \boldsymbol{A}(\boldsymbol{x})\boldsymbol{x} + \boldsymbol{B}(\boldsymbol{x})\boldsymbol{u}(\boldsymbol{x})\ , \quad (7)$$

provided that the nonlinear system has an equilibrium at the origin, i.e. $\boldsymbol{f}(\boldsymbol{0}, \boldsymbol{0}) = \boldsymbol{0}$ and the Jacobian matrices of matrices $\boldsymbol{A}(\boldsymbol{x})$ and $\boldsymbol{B}(\boldsymbol{x})$ are subject to Lipschitz condition of bounded growth (Harrison, 2003). Then the nonlinear optimal control can be extended from the linear method explained in Section 3.1 in the following steps.

First, a generalised quadratic infinite time optimal cost function can be defined as:

$$J = \frac{1}{2}\int_0^\infty [\boldsymbol{x^T Q}(\boldsymbol{x})\boldsymbol{x} + \boldsymbol{u^T R}(\boldsymbol{x})\boldsymbol{u}]dt$$

and when attached to the nonlinear system governed by Eq. (7), generates the nonlinear optimal control:

$$\boldsymbol{u} = -\boldsymbol{K}(\boldsymbol{x})\boldsymbol{x} = -\boldsymbol{R^{-1}}(\boldsymbol{x})\boldsymbol{B^T}(\boldsymbol{x})\boldsymbol{P}(\boldsymbol{x})\boldsymbol{x}\ , \quad (8)$$

where $\boldsymbol{P}(\boldsymbol{x})$ must satisfy the extended algebraic Riccati equation shown as follows:

$$\boldsymbol{A^T}(\boldsymbol{x})\boldsymbol{P}(\boldsymbol{x}) + \boldsymbol{P}(\boldsymbol{x})\boldsymbol{A}(\boldsymbol{x}) + \boldsymbol{Q}(\boldsymbol{x}) - \boldsymbol{P}(\boldsymbol{x})\boldsymbol{B}(\boldsymbol{x})\boldsymbol{R^{-1}}(\boldsymbol{x})\boldsymbol{B^T}(\boldsymbol{x})\boldsymbol{P}(\boldsymbol{x}) = \boldsymbol{0}\ . \quad (9)$$

Next, substitute the nonlinear optimal control solution shown in Eq. (8) into Eq. (7), the system model results in:

$$\dot{\boldsymbol{x}} = \left[\boldsymbol{A}(\boldsymbol{x}) - \boldsymbol{B}(\boldsymbol{x})\boldsymbol{R^{-1}}(\boldsymbol{x})\boldsymbol{B^T}(\boldsymbol{x})\boldsymbol{P}(\boldsymbol{x})\right]\boldsymbol{x}. \quad (10)$$

Finally, Eq. (10) can be solved numerically, using an integration method, where $\boldsymbol{A}(\boldsymbol{x})$, $\boldsymbol{B}(\boldsymbol{x})$, $\boldsymbol{B^T}(\boldsymbol{x})$, $\boldsymbol{R^{-1}}(\boldsymbol{x})$ and $\boldsymbol{P}(\boldsymbol{x})$ are fixed (frozen) at each time step. This method can therefore be referred to as the 'nonlinear freezing optimal control - NFOC' for this reason. Note, in the linear quadratic regulating or tracking control cases explained in Section 3.1, the optimal control gain matrix $\boldsymbol{K}$ was obtained by performing the optimisation once and then applied to the linearised system for all time. Differently, in the nonlinear optimal freezing control, an optimisation is performed and therefore results in a varying $\boldsymbol{K}(\boldsymbol{x})$ at every time step. Generally, as the linear optimal gain matrix was calculated based the linearised model around a small neighbourhood of

the equilibrium, the control will only function as intended when the system is restricted within this neighbourhood. In comparison, the nonlinear freezing technique is far more flexible and can control globally where $\boldsymbol{A}(\boldsymbol{x})$ and $\boldsymbol{B}(\boldsymbol{x})$ are a stabilisable pair.

The numerical procedure of calculating the nonlinear optimisation solution of the control gain matrix $\boldsymbol{K}(\boldsymbol{x})$ can be summarised as follows:

1) Use the initial state vector $\boldsymbol{x}(\boldsymbol{0})$ to determine matrices $\boldsymbol{A}(\boldsymbol{x}(\boldsymbol{0}))$ and $\boldsymbol{B}(\boldsymbol{x}(\boldsymbol{0}))$ at time step $t = 0$.
2) Solve the algebraic Riccati equation shown in Eq. (9) to obtain $\boldsymbol{P}\big(\boldsymbol{x}(\boldsymbol{0})\big)$ and then substitute it into Eq. (8) to determine the optimal control gain matrix for the initial time step $\boldsymbol{K}\big(\boldsymbol{x}(\boldsymbol{0})\big)$.
3) Substitute $\boldsymbol{A}(\boldsymbol{x}(\boldsymbol{0}))$, $\boldsymbol{B}(\boldsymbol{x}(\boldsymbol{0}))$ and $\boldsymbol{P}\big(\boldsymbol{x}(\boldsymbol{0})\big)$ into Eq. (10) and use an integration method (e.g. a 4th order Runge-Kutta method) to solve for $\boldsymbol{x}$ at the next time step $t = 1$, say $\boldsymbol{x}(\boldsymbol{1})$.
4) Repeat steps 1) - 3) using $\boldsymbol{x}(\boldsymbol{1})$ to work out the optimal control gain matrix at $t = 1$ as $\boldsymbol{K}\big(\boldsymbol{x}(\boldsymbol{1})\big)$ and then move onto the next time step following the same procedure.

This nonlinear freezing technique (see (Banks and Mhana, 1992) and (McCaffrey and Banks, 2001) for detailed derivation and theoretical analysis) will be applied to the TWR system to provide stabilising and tracking controls. In the next section, the nonlinear state-space model of the TWR system given in Eq. (3) will used and simulation results from this nonlinear control will be compared with the linear tracking control extended from the traditional LQR method.

4 Simulation Results and Discussions

4.1 Controllability Tests

State-space representations of dynamical systems have non-unique forms and controllability (or at least, stabilisability) is a necessary condition of controller design in state-space. For a linear system, as matrices $\boldsymbol{A}$ and $\boldsymbol{B}$ are time-invariant, controllability of any state-space model is fixed and can be tested straightforwardly. For a nonlinear system and any given state-space model, however, matrices $\boldsymbol{A}(\boldsymbol{x})$ and $\boldsymbol{B}(\boldsymbol{x})$ both depend on the state vector $\boldsymbol{x}$ and therefore vary.

Using the nonlinear state-space model derived in Eq. (3) of a tracking TWR system, where matrices $\boldsymbol{A}(\boldsymbol{x})$ and $\boldsymbol{B}(\boldsymbol{x})$ depend on the state variables x_3 and x_4 only, the controllability information can be obtained as shown in Figure 2 where the TWR system is fully controllable when the values of state variables x_3 and x_4 lie in the yellow region representing Rank($\boldsymbol{\mathcal{C}}$) = 5, where the controllability test matrix $\boldsymbol{\mathcal{C}} = [\boldsymbol{B}(\boldsymbol{x}) \vdots \boldsymbol{A}(\boldsymbol{x})\boldsymbol{B}(\boldsymbol{x}) \vdots \boldsymbol{A}(\boldsymbol{x})^2\boldsymbol{B}(\boldsymbol{x}) \vdots \boldsymbol{A}(\boldsymbol{x})^3\boldsymbol{B}(\boldsymbol{x}) \vdots \boldsymbol{A}(\boldsymbol{x})^4\boldsymbol{B}(\boldsymbol{x})]$. In the blue region, Rank($\boldsymbol{\mathcal{C}}$) = 4, the TWR system has a controllability rank deficiency and therefore is not completely state controllable.

Clearly, if a different state-space model than the one shown in Eq. (3) is adopted for the TWR system, the controllability dependence on the state vector will vary accordingly.

4.2 Control Results and Comparisons

In this section, the control performance and controllable range of the NFOC design of the TWR system will be examined, comparing against LOC, in simulations conducted in MATLAB environment. The weighting matrices are chosen as $\boldsymbol{Q} = diag\{20, 1, 1, 1, 5\}$ and $\boldsymbol{R} = 10\boldsymbol{I_{2\times 2}}$ after some simple trial and error tests. The weighting matrices are then kept the same for all simulation runs when using both the NFOC and LOC techniques.

Using the NFOC theory and numerical procedure explained in Section 3.2, the tracking control of wheel angular displacement x_1 (when the reference input is 2π or 360°) and the stabilising control results of the TWR system with different initial pitch angle x_3 can be shown in Figures 3 and 4, respectively. For the ease of interpretation, units of all angles have been converted from radians to degrees (°). Note all state variables in Figure 3 and all other state variables apart from x_3 in Figure 4 have zero initial conditions.

It can be seen from Figure 3 that the designed nonlinear freezing optimal controller has the ability to track reference input in x_1 well with a settling time at ~8s. The performance of the linear optimal controller is comparable to the one by NFOC.

In Figure 4, as the initial pitch angle of the robot body increases, as one would expect, the maximum oscillation amplitudes of all state variables (physically, the wheel angular placement, the wheel angular velocity, the body pitch angle, the pitch angular velocity and the accumulation of translational displacement) and the corresponding control input get larger. It can also be seen from Figure 4 that the time taken to stabilise the TWR rises when the pitch angle x_3 increases, however, the NFOC is capable of stabilising the TWR system starting from a wide range of initial pitch angles. This is because for these initial x_3 angles, the controllability trajectories due to dynamical evolutions of state variables x_3 and x_4 stay within the controllable region. A typical example is shown in Figure 5, where the red asterisks represent the rank test results for specific x_3 and x_4 values which evolved from initial condition $x_3 = 30^{\circ}$, $x_4 = 0^{\circ}/s$ and the TWR system controlled by the nonlinear optimal technique.

When the pitch angle x_3 increases further to 87.2° whilst all other state variables remain 0 initially, the controlled response of TWR using NFOC is only just stable, with dramatic fluctuations and very large

maximum oscillation amplitudes for all state variables, as shown in Figure 6. The controllability results for this case are shown in Figure 7. It can be seen that the red asterisks which represent the dynamical evolution path of state variables x_3 and x_4 still remain in the yellow controllable region, where the controllability test matrix is of full rank.

The control results shown in Figures 3, 4 and 6 are achieved through simulations which demonstrate the theoretical capability of the NFOC. These results will be compared against the ones obtained from using the LOC in later part of this section to show the superiority of NFOC in achieving stabilisation of much wider ranges of important state variables and robustness. Although the simulation results are stable, clearly, when implementing TWR, hardware constraints will apply which means the control inputs and some variables may exceed their physical limits. For example, in Figures 4 and 6, the peak control voltages demanded by the NFOC when initial $x_3 = 60^{\circ}$ and 87.2° are $\sim 110V$ and $\sim 750V$, respectively, which are much larger than voltage supplied by any existing Lego motors and indeed, by most motors used in robotics. The peak pitch angular velocities of the robot body are $\sim -1500^{\circ}/s$ and $> 9000^{\circ}/s$ (also $< -9000^{\circ}/s$), respectively, which are also physically unrealistic to achieve. Further design and experiments which limit the control voltage supplied is necessary to make the results more physically meaningful and will be demonstrated in Section 4.3.

For now, the controllable range of the TWR from the model identified in Eq. (3) is tested for the NFOC method. When the initial robot pitch angle x_3 is increased to 87.3°, the system becomes unstable, as shown by simulation results in Figure 8.

Similarly as before, the controllability results can be displayed, tracing the dynamical evolution path of x_3 and x_4 starting from $x_3 = 87.3^{\circ}$, as shown in Figure 9. This time, however, the state variables travel into the blue region, where the controllability test matrix $\boldsymbol{\mathcal{C}}$ has a rank deficiency of 1 (i.e. Rank($\boldsymbol{\mathcal{C}}$) = 4). Because the system is not fully controllable at these specific values of the state variables, as one would expect, the TWR cannot be stabilised using any state-space control technique, including the NFOC method. This controllability conclusion matches the results of unstable state variable evolutions against time, shown in Figure 8.

It can also be shown in Figure 10 that when the initial value for x_3 is further increased to 90°(i.e. the robot is lying flat down on the horizontal surface), the TWR system is not fully controllable at a number of values on the state variables dynamical evolution path, and therefore it cannot be stabilised.

Next, stabilising ranges between the NFOC and the LOC methods are compared. LOC is an extended tracking control method based on the powerful LQR technique briefly explained in Section 3.1, where a set of optimal control gains are calculated for the linearised model of the system. The approximations made at the linearisation stage restrict the operational range of the system to be within a small neighbourhood of the equilibrium. In the case of the TWR system, the equilibrium sits in the robot's upright position with zero pitch angular velocity.

The LOC method can perform excellent tracking and stabilising control when the state variables stay within the operational range (close to the equilibrium). For example, when the initial robot pitch angle is 5°, the LOC control results are nearly identical to the ones generated by the NFOC method, as shown in Figure 11. Indeed, the set of linear optimal control gains $\boldsymbol{K_l}$ calculated as shown below:

$\boldsymbol{K_l} = [-1.391, -1.449, -59.848, -7.168, -0.5]$,

are very similar to the ones obtained for the nonlinear case. Nonlinear freezing optimal control gains $\boldsymbol{K_n}(\boldsymbol{x})$ vary depending on the state vector $\boldsymbol{x}$, so a subset of the gains calculated is shown in Table 4.1 for different corresponding values of x_3, where x_1, x_2, x_4 and x_5 are all set at 0.

However, when the state variables of the TWR either start initially at or subsequently travel into, any region outside the small neighbourhood of the equilibrium, the control performed by LOC is no longer optimal, even when the system is still fully controllable. This restriction does not apply to the NFOC method, because it is a nonlinear control method in which a new set of optimal control gains is calculated, updated and utilised for control at every time step. The advantage of the NFOC technique is therefore that it can achieve optimal control of any nonlinear system (subject to the condition that $\boldsymbol{A}(\boldsymbol{x})$ and $\boldsymbol{B}(\boldsymbol{x})$ are a stabilisable pair) globally. In addition, because the optimal control gains are calculated and refreshed at every time step, taking into account of effects of any disturbances, the system is intrinsically more robust.

It has already been demonstrated that the NFOC technique can control the TWR system from a large range of initial values of the most unstable variable - the robot body's pitch angle, up to $x_3 = 87.2^{\circ}$. This represents a much wider range than shown in other recent simulation work on TWR (Guo et. al. 2021) and inverted pendulum control (Maity and Luecke, 2019). In Figure 12, the stabilising control results between the NFOC and the LOC methods are compared, at a lower initial pitch angle at $x_3 = 65.7^{\circ}$, as the LOC cannot provide stabilising control exceeding this angle. Even though the LOC is still able to control the TWR starting from $x_3 = 65.7^{\circ}$, Figure 12 shows more oscillatory

responses with nearly always larger peak amplitudes of the state variables, comparing against the NFOC method.

When the robot body pitch angle is further increased to 65.8°, the TWR controlled by LOC is unstable, as shown in Figure 13, whilst the stabilising control performance by NFOC is still satisfactory, as shown in Figure 14.

4.3 Control Saturations

As discussed in Section 4.2, there are physical limits of voltages, a Lego EV3 motor, or indeed, any motor used in robotics research, could supply for the TWR. In order to consider the effect of the motor voltage limitation, the model of the TWR needs to be modified to take into account of this constraint. Harrison's (2003) scalar input state augmentation approach is adopted and extended to a vector input state augmentation, as two motors are utilised in TWR and therefore generating two control inputs.

Now for the TWR system, let:

$$\boldsymbol{\phi}(x_6) = \begin{bmatrix} \phi_L(x_6) \\ \phi_R(x_6) \end{bmatrix} = \boldsymbol{u} = \begin{bmatrix} v_1 \\ v_2 \end{bmatrix}$$

and define the additional state variable x_6 such that

$$\dot{x}_6 = w,$$

then the extended TWR model can be rewritten as:

$$\dot{\boldsymbol{x}}_{\boldsymbol{c}} = \begin{bmatrix} \dot{\boldsymbol{x}} \\ \dot{x}_6 \end{bmatrix} = \begin{bmatrix} \boldsymbol{A}(\boldsymbol{x}) & \frac{\boldsymbol{B}(\boldsymbol{x})\boldsymbol{\phi}(x_6)}{x_6} \\ 0_{1\times n} & 0 \end{bmatrix} \begin{bmatrix} \boldsymbol{x} \\ x_6 \end{bmatrix} + \begin{bmatrix} 0_{n\times 1} \\ 1 \end{bmatrix} w, \tag{16}$$

where $\dot{\boldsymbol{x}}_{\boldsymbol{c}} = [\dot{x}_1, \dot{x}_2, \dot{x}_3, \dot{x}_4, \dot{x}_5, \dot{x}_6]^T$ and w is the new 'artificial' (non-physical) scalar control input. The control saturation vector $\boldsymbol{\phi}(x_6)$ can be defined as any smooth and differentiable functions, for example, by using the one introduced in (Harrison, 2003) as follows:

$$\phi_L(x_6) = \phi_R(x_6) = \begin{cases} \lambda\ , & x_6 > \lambda \\ \lambda sin\left(\frac{\pi x_6}{2\lambda}\right), & |x_6| \geq \lambda \\ -\lambda\ , & x_6 < -\lambda \end{cases},$$

where λ denotes the maximum motor voltage of the TWR. For a Lego EV3 motor, this value is 8.3V.

The full state-space model of the extended TWR with the motor voltages constraint embedded can be obtained by substituting Eq. (3) into Eq. (16), giving the following state-space representation:

$$\dot{\boldsymbol{x}}_{\boldsymbol{c}} = \boldsymbol{A}_{\boldsymbol{c}}(\boldsymbol{x}_{\boldsymbol{c}})\boldsymbol{x}_{\boldsymbol{c}} + \boldsymbol{B}_{\boldsymbol{c}}(\boldsymbol{x}_{\boldsymbol{c}})w, \tag{17}$$

where

$$\boldsymbol{A}_{\boldsymbol{c}} = \begin{pmatrix} 0 & 1 & 0 & 0 & 0 & 0 \\ 0 & \frac{e_{m22}}{a+b} & \frac{e_{m23}}{(a+b)x_3} & \frac{e_{m24}}{a+b} & 0 & \frac{f_{m21}\phi_L(x_6)+f_{m22}\phi_R(x_6)}{(a+b)x_6} \\ 0 & 0 & 0 & 1 & 0 & 0 \\ 0 & \frac{e_{m42}}{a+b} & \frac{e_{m43}}{(a+b)x_3} & \frac{e_{m44}}{a+b} & 0 & \frac{f_{m41}\phi_L(x_6)+f_{m42}\phi_R(x_6)}{(a+b)x_6} \\ 1 & 0 & 0 & 0 & 0 & 0 \\ 0 & 0 & 0 & 0 & 0 & 0 \end{pmatrix}$$

and $\boldsymbol{B}_{\boldsymbol{c}} = [0, 0, 0, 0, 0, 1]^T$. Thus, the quadratic infinite time optimal cost function becomes:

$$J = \frac{1}{2}\int_0^{\infty} [\boldsymbol{x}_{\boldsymbol{c}}{}^{\boldsymbol{T}}\boldsymbol{Q}_{\boldsymbol{c}}(\boldsymbol{x}_{\boldsymbol{c}})\boldsymbol{x}_{\boldsymbol{c}} + w^T\boldsymbol{R}_{\boldsymbol{a}}(\boldsymbol{x}_{\boldsymbol{c}})w]dt,$$

where the control weighting matrix $\boldsymbol{R}_{\boldsymbol{a}}$ is now a scalar quantity due to the new scalar control input adopted and is chosen to be $R_a = 0.001$ and the state weighting matrix $\boldsymbol{Q}_{\boldsymbol{c}}$ is given by

$$\boldsymbol{Q}_{\boldsymbol{c}} = \begin{bmatrix} \boldsymbol{Q} & 0 \\ 0 & 2\phi_L^2(x_6)\boldsymbol{R}_{11} \end{bmatrix},$$

with $\boldsymbol{Q}$ and $\boldsymbol{R}$ chosen to be the same as in Section 4.2, i.e. $\boldsymbol{Q} = diag\{20, 1, 1, 1, 5\}$ and $\boldsymbol{R} = 10\boldsymbol{I}_{\boldsymbol{2\times 2}}$ (so $\boldsymbol{R}_{11}$ = 10).

Now because the state-space model of the TWR has changed with the motor voltage constraint embedded, controllability of the system also changed but can be analysed using the same method as explained in Section 4.2.

Rank of the new controllability test matrix depends on 3 state variables of the new TWR model with motor voltage input saturations, as shown in Figure 15. Same as before, the yellow region represents fully controllable states (i.e. Rank($\boldsymbol{\mathcal{C}}$) = 6) and the blue region represents partly controllable states (i.e. Rank($\boldsymbol{\mathcal{C}}$) = 5 so there is a controllability rank deficiency of 1).

Cross-sections of the controllability cuboid presented in Figure 15 can be plotted to better visualise the dynamical evolution path of the state variables, when 1 of the 3 state variables x_3, x_4 and x_6 is fixed. For example, when x_4 is fixed at $x_4 = 0^{\circ}/s$, the controllability information, in terms of x_3 and x_6 can be captured and visualised more easily as shown in Figure 16. Note, the coordinates (x_3, x_6) of the 2 points marked by red asterisks are approximated as $(-90°, -8.4 \times 10^{15})$ and $(90°, 8.6 \times 10^{15})$, which indicate the boundaries of the fully controllable range. Similarly, if x_3 is fixed at $x_3 = 0^{\circ}$, the controllability information can be presented by the cross-sectional plot shown in Figure 17, where the coordinates (x_4, x_6) of the 2 points marked by red asterisks are $(-200\ °/s, -8.4 \times 10^{15})$ and $(-200\ °/s,\ 8.6 \times 10^{15})$.

When the maximum motor voltage λ is increased, as one would expect, the larger the stabilising control range of the robot pitch angle x_3 can be achieved, using the NFOC method with embedded control saturations. For example, if a motor - Maxon series EC 60 flat with a nominal voltage 48V and a high nominal torque 298 mNm (Maxongroup, 2012) is selected, the TWR system's controllability is shown in Figure 18.

Simulation experiments show that with $\lambda = 48V$, the NFOC technique can stabilise the TWR robot pitch angle x_3, up to 88.0°, as shown in Figure 19. Although the motor voltage has a maximum value of 48V, the nonlinear optimal control performance compares

favourably against the situation when there was no motor voltage saturation, as plotted in Figure 6. Here as shown in Figure 19, all state variables show less oscillatory evolutions than in Figure 6. The TWR robot has returned to the upright position from a very large initial pitch angle in less than $2s$ and the settling time for the wheel angle displacement is approximately $6s$.

As one would expect, the NFOC with the motor voltage saturated at 48V can achieve better stabilisation performance than the LOC method with the same control saturation, for the TWR system. When control saturations of ± 48V are applied to the linearised TWR system given by Eq. (4), the LOC technique can be shown to stabilise the robot body pitch angle, up to 56.3°. The LOC and NFOC controlled responses of state variables when the TWR started from $x_3 = 56.3^{\circ}$ are presented in Figure 20 and although stable, the LOC controlled responses are very oscillatory in comparison with the NFOC one. When x_3 exceeds this angle, LOC cannot provide sufficient control and the system becomes unstable. Therefore, it is demonstrated that NFOC achieves a much larger stabilisation range and more stable responses than LOC in x_3 for the TWR system, when motor voltage is saturated at ± 48V.

NFOC is an intrinsically robust control technique due to its nature of generating state-vector dependent control solutions. Typical robustness tests include the introduction of model uncertainties and external disturbances (Huang et. al. 2019b). Here, the TWR is subject to a 0.12kg body mass and a 5cm height increment, representing model uncertainties fluctuating to 18.75% of additional mass and 23.81% of additional height, respectively. Control results of the TWR from using both LOC and NFOC are depicted in Figure 21 where the maximum stabilisation angle of 36.4° (comparing against 56.3° without modelling uncertainties) for LOC is reached. It is also clear that the LOC responses are much more oscillatory than the NFOC ones. Figure 22 shows using NFOC can achieve a maximum stabilisation angle of 77.6° (comparing against 88.0° without modelling uncertainties), which demonstrates NFOC's capability in the existence of large modelling uncertainties and that NFOC is more robust than LOC.

5 Conclusions

In this paper, a TWR constructed using Lego EV3 components was used as a prototype to test the effectiveness of a nonlinear stabilising optimal control technique - NFOC. A nonlinear state-space model of the TWR was obtained using the Lagrangian method and then extended to a tracking system model to facilitate successful achievement of an extra control objective of following a pre-defined wheel angular displacement reference, on top of the self-balancing control of robot body. The control strategy and numerical procedure of the NFOC were presented and applied to the TWR system. Simulation results demonstrated superior stabilisation ability of the NFOC, not only covering a much wider range of the robot body pitch angle x_3, (up to 87.2°), comparing against the LOC (up to 65.7°) and other results in recent literature (Guo, Rizvi and Lin, 2021) and (Maity and Luecke, 2019), but also providing less oscillatory responses when x_3 is large. The stabilisation outcome was consistent when the motor voltage saturations were taken account of and the complexity of the TWR model was increased. Furthermore, the robustness tests demonstrated NFOC could still achieve excellent stabilisation outcome when the TWR had large model uncertainties. These results were significant as the achieved control range of the robot pitch angle was larger than any other methods reported in the literature and demonstrated that the NFOC was a truly global controller.

Future work will include practical implementations of the NFOC and the LOC for the Lego EV3 TWR system for comparison. Extended Kalman filter designs will also be conducted in order to remove sensor noises.

Figure 1 A two-wheel robot constructed with LEGO EV3 (a) side view; (b) top view

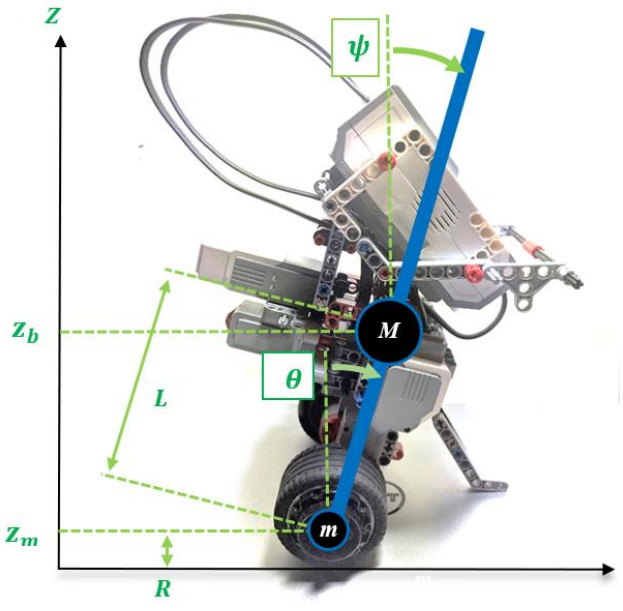

(a)

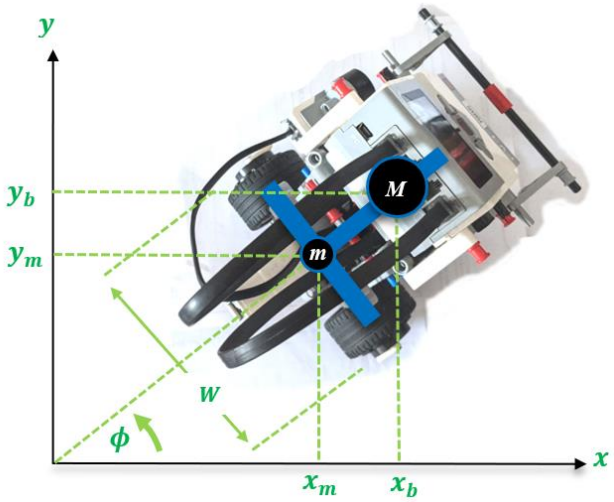

(b)

Figure 2 Rank of Controllability Test Matrix of the TWR model

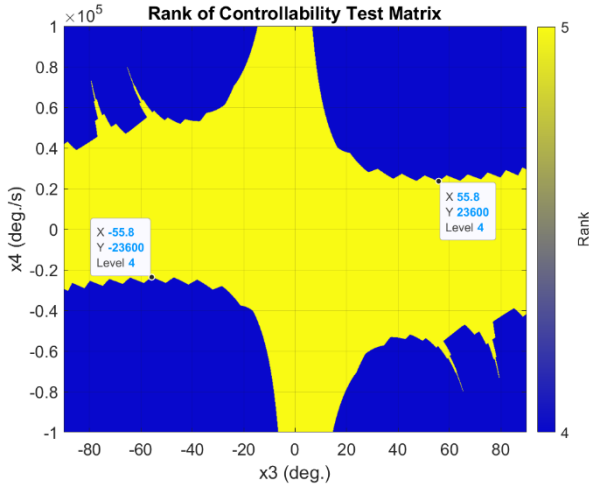

Figure 3 The tracking controls of x_1 of TWR using NFOC and LOC

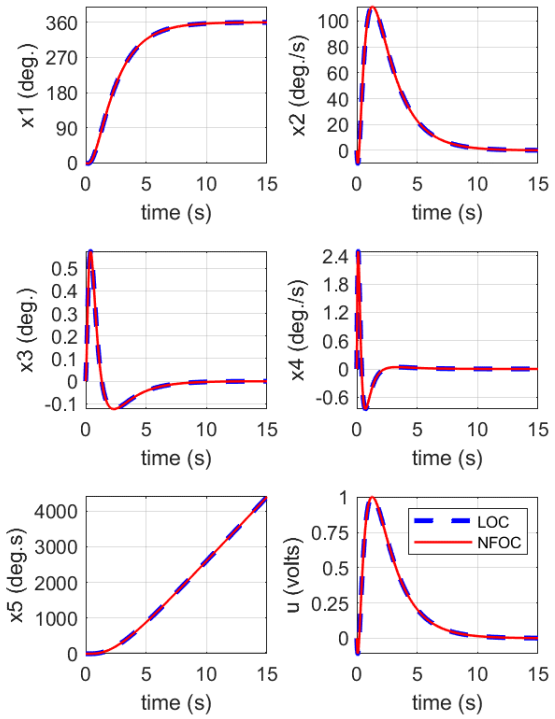

Figure 4 The stabilising controls of TWR using NFOC from varying initial x_3 shown in the legend

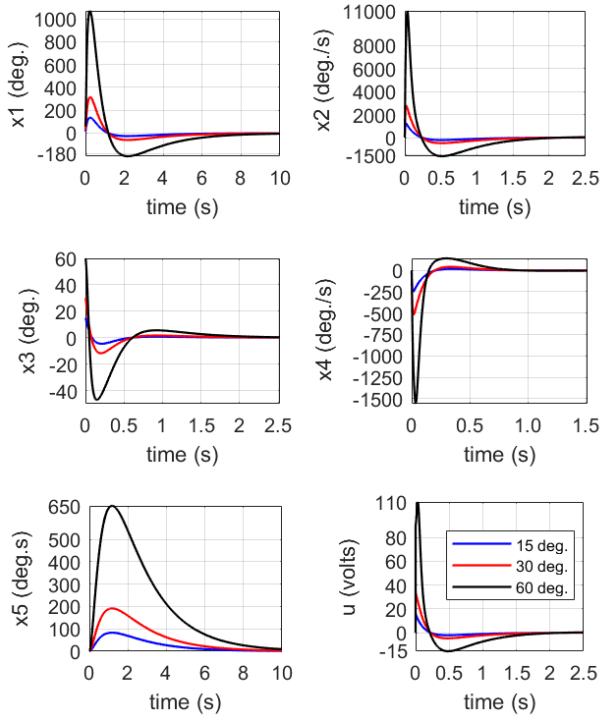

Figure 5 Rank of Controllability Test Matrix and dynamical evolutions of x_3 and x_4, starting from $x_3 = 30^\circ$ and $x_4 = 0^\circ/s$, controlled by NFOC

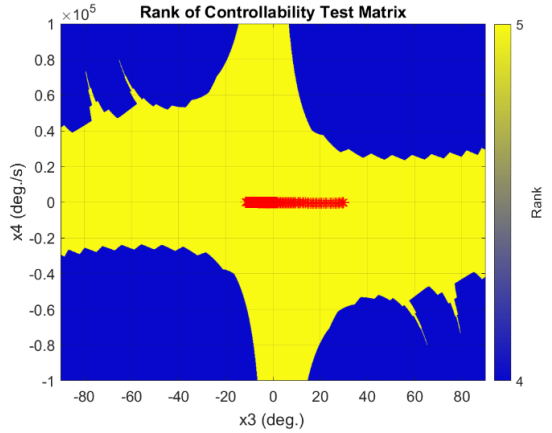

Figure 7 Rank of Controllability Test Matrix and dynamical evolutions of x_3 and x_4, starting from $x_3 = 87.2^\circ$,controlled by NFOC

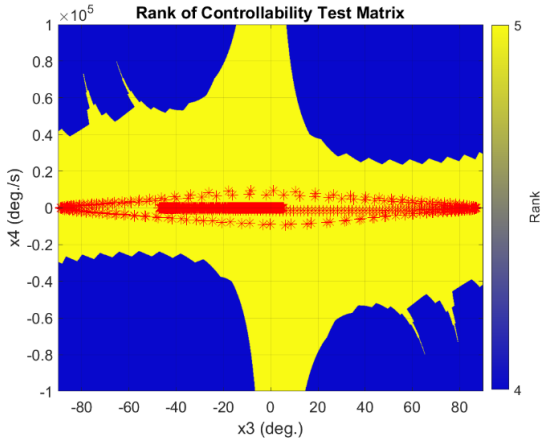

***Figure* 6** *The stabilisation of TWR using NFOC from initial pitch angle* $x_3 = 87.2^\circ$

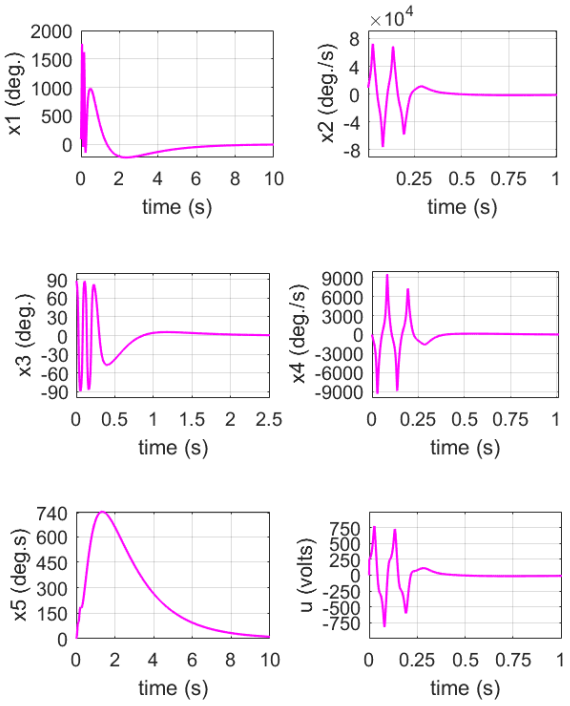

***Figure* 8** *Uncontrollable system from the initial pitch angles* $x_3 = 87.3^\circ$*, using NFOC*

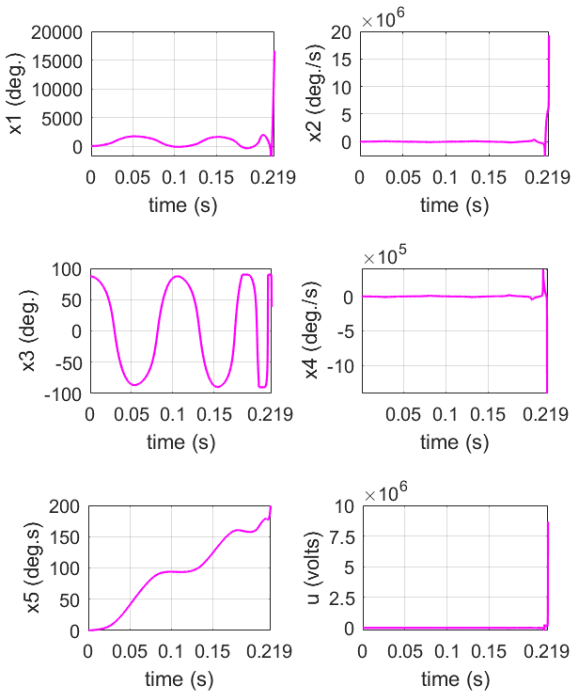

Figure 9 Rank of Controllability Test Matrix and dynamical evolutions of x_3 and x_4, starting from $x_3 = 87.3^{\circ}$,controlled by NFOC

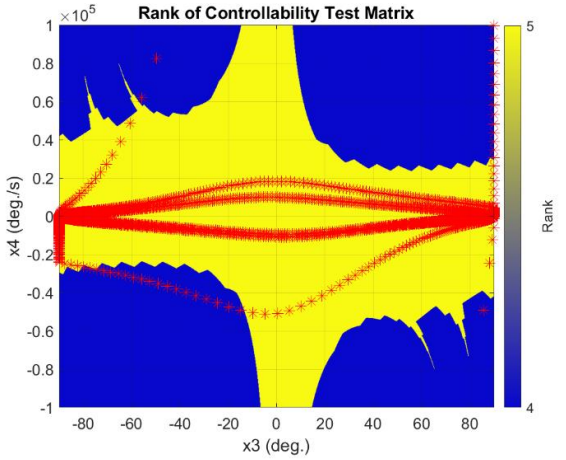

Figure 10 Rank of Controllability Test Matrix and dynamical evolutions of x_3 and x_4, starting from $x_3 = 90^{\circ}$, controlled by NFOC

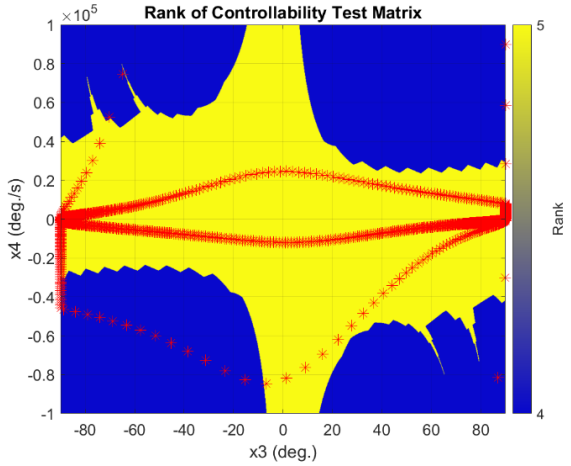

Figure 11 Stabilisation of the TWR using LOC and NFOC methods from initial pitch angle $x_3 = 5^{\circ}$

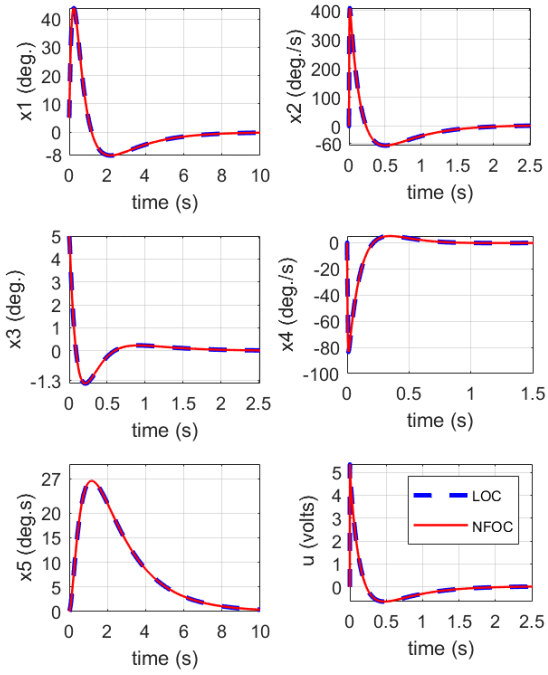

Figure 12 Stabilisation of the TWR using LOC and NFOC methods from initial pitch angle $x_3 = 65.7^{\circ}$

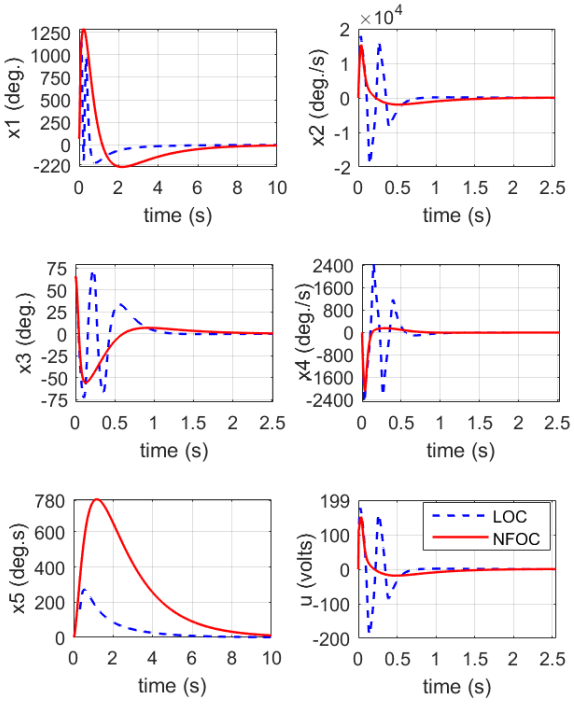

Figure 13 Unstable performance of the TWR controlled by LOC from initial pitch angle $x_3 = 65.8^{\circ}$

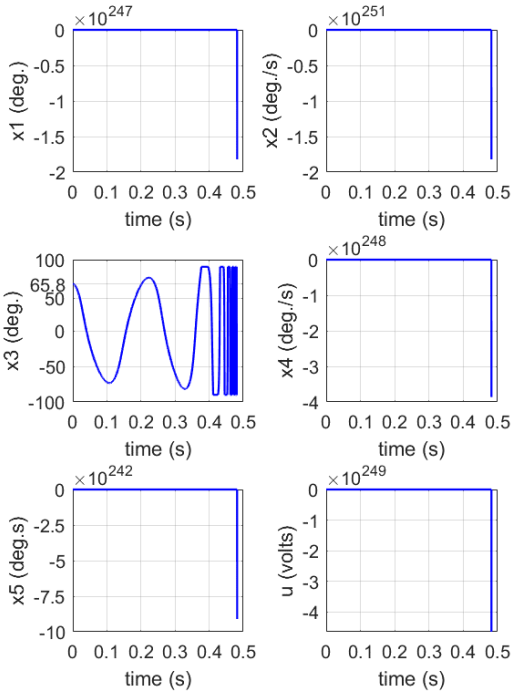

Figure 14 Stable performance of the TWR controlled by NFOC from initial pitch angle $x_3 = 65.8^{\circ}$

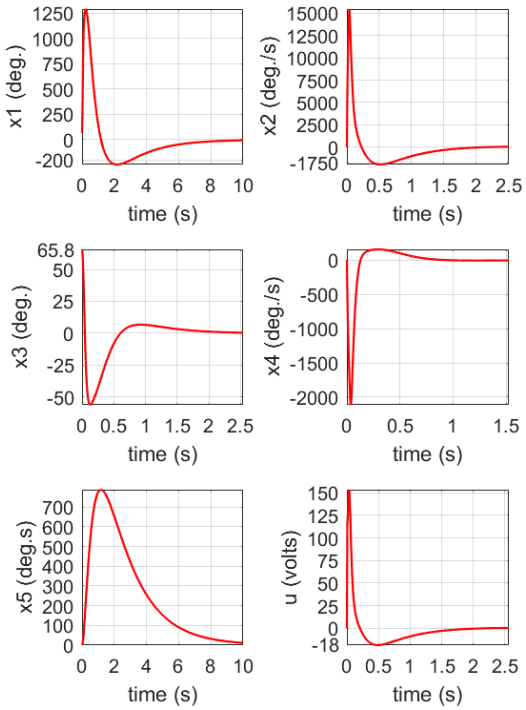

Figure 15 Rank of Controllability Test Matrix of the TWR model with motor voltage input saturations

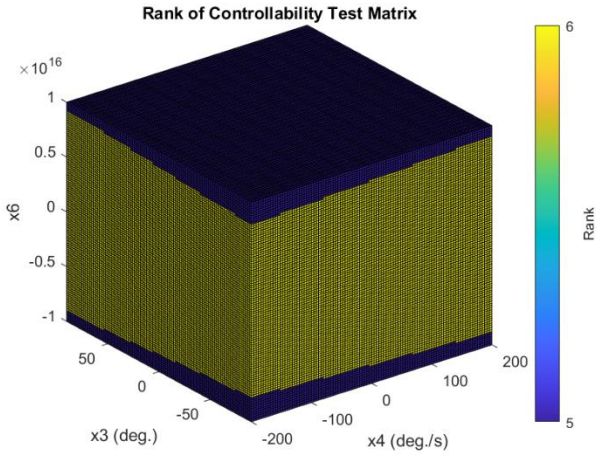

Figure 16 Rank of Controllability Test Matrix Cross-sectional Plot when x_4 is fixed at $x_4 = 0^{\circ}/s$

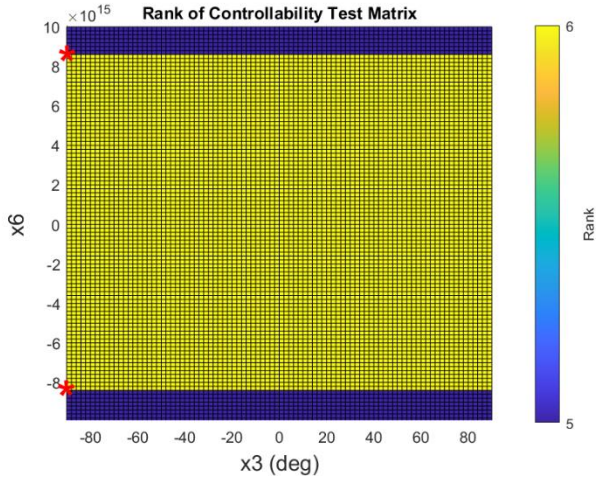

Figure 17 Rank of Controllability Test Matrix Cross-sectional Plot when x_3 is fixed at $x_3 = 0^{\circ}$

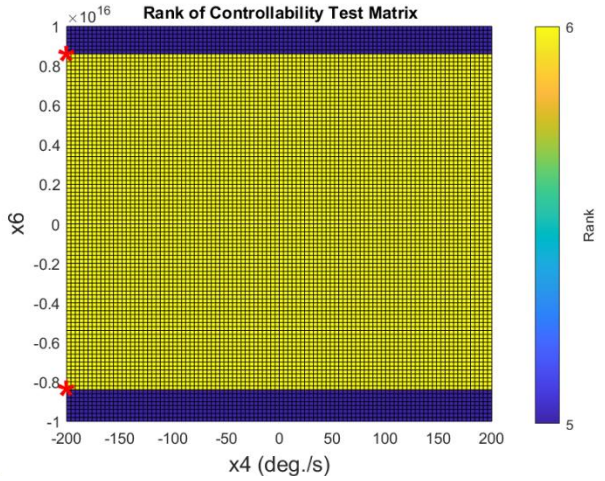

Figure 18 Rank of Controllability Test Matrix of the TWR model with motor voltage input saturated at 48V

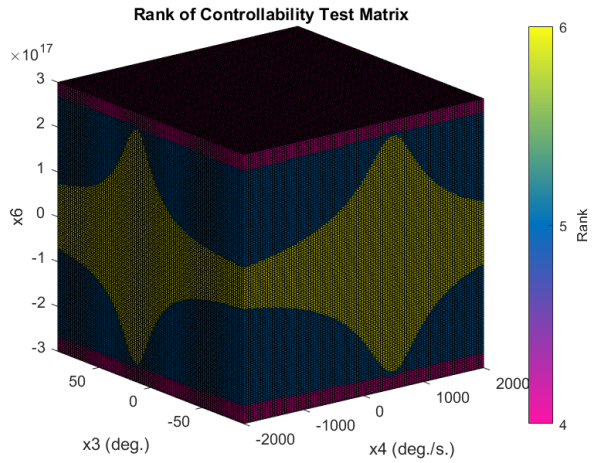

Figure 19 The stabilisation of TWR with control saturated at 48V using NFOC, from initial pitch angle x_3= 88.0˚

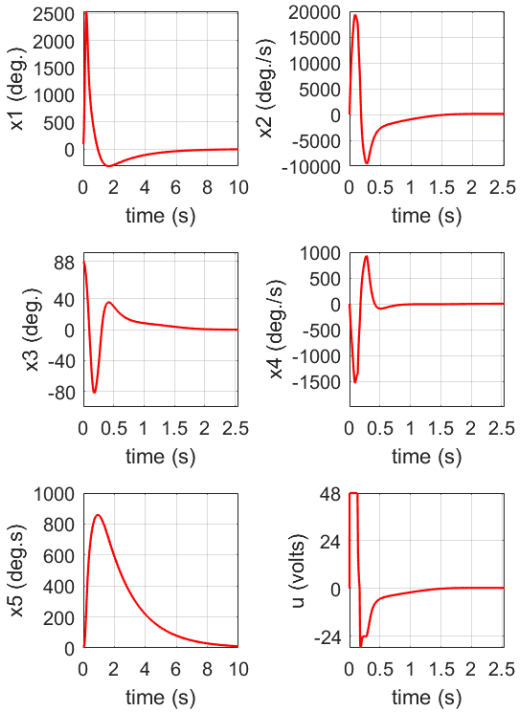

Figure 20 The stabilisation of TWR with control saturated at 48V using LOC and NFOC, from initial pitch angle x_3= 56.3˚

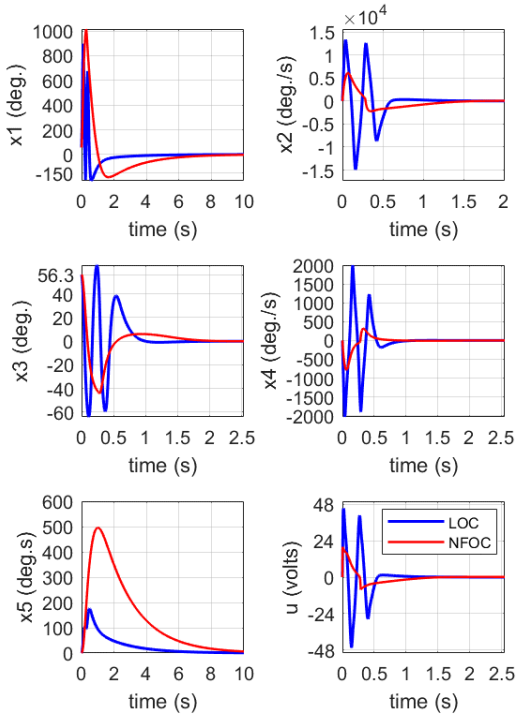

Figure 21 The stabilisation of TWR when subject to model uncertainties with control saturated at 48V using LOC and NFOC, from initial pitch angle x_3= 36.4˚

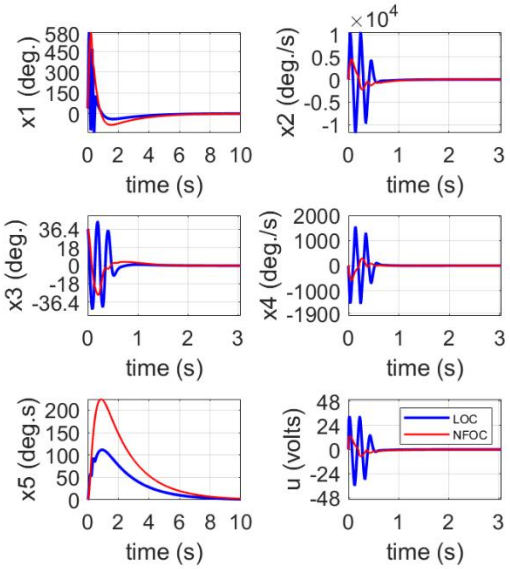

Figure 22 The stabilisation of TWR when subject to model uncertainties with control saturated at 48V using NFOC, from initial pitch angle $x_3 = 76.6^{\circ}$

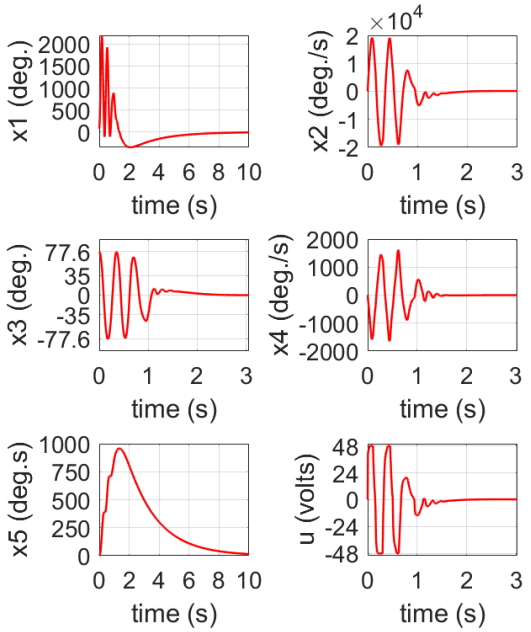

Table 4.1 NFOC gains $\boldsymbol{K_n(x)}$ for a small range of x_3

x_3	$\boldsymbol{K_n(x)}$
$\pm 5^{\circ}$	$[-1.391, -1.449, -59.968, -7.187, -0.5]$
$\pm 4^{\circ}$	$[-1.391, -1.449, -59.925, -7.180, -0.5]$
$\pm 3^{\circ}$	$[-1.391, -1.449, -59.891, -7.175, -0.5]$
$\pm 2^{\circ}$	$[-1.391, -1.449, -59.867, -7.171, -0.5]$
$\pm 1^{\circ}$	$[-1.391, -1.449, -59.852, -7.169, -0.5]$
0°	$[-1.391, -1.449, -59.848, -7.168 - 0.5]$

Acknowledgment

The first author would like to thank the Royal Thai Government and the Synchrotron Light Research Institute (SLRI) (public organisation), Thailand for the scholarship funding.

References

Banks, S. P., & Mhana, K. J. (1992). Optimal control and stabilization for nonlinear systems. *IMA Journal of Mathematical Control and Information*, *9*(2), pp. 179-196.

Boubaker, O. (2013). The inverted pendulum benchmark in nonlinear control theory: a survey. *International Journal of Advanced Robotic Systems*, *10*(5), pp. 233.

Elkinany, B., Mohammed, A., Krafes, S., & Chalh, Z. (2020). Backstepping controller design with a quadratic error for a double inverted pendulum. *International Journal of Modelling, Identification and Control*, 34(1), 33-40.

Grasser, F., D'Arrigo, A., Colombi, S., & Rufer, A. C. (2002). JOE: A mobile, inverted pendulum. *IEEE Transactions on Industrial Electronics*, 49(1), 107-114.

Guo, L., Rizvi, S. A. A., & Lin, Z. (2021). Optimal control of a two-wheeled self-balancing robot by reinforcement learning. *International Journal of Robust and Nonlinear Control*, 31(6), 1885-1904.

Harrison, R. F. (2003). Asymptotically optimal stabilising quadratic control of an inverted pendulum. *IEE Proceedings-Control Theory and Applications*, *150*(1), pp. 7-16.

Huang, J., Zhang, T., Fan, Y., & Sun, J. Q. (2019a). Control of rotary inverted pendulum using model-free backstepping technique. *IEEE Access*, 7, 96965-96973.

Huang, J., Zhang, M., Ri, S., Xiong, C., Li, Z., & Kang, Y. (2019b). High-order disturbance-observer-based sliding mode control for mobile wheeled inverted pendulum systems. *IEEE Transactions on Industrial Electronics*, 67(3), 2030-2041.

Jasim, W., & Gu, D. (2018). Robust path tracking control for quadrotors with experimental validation. International Journal of Modelling, *Identification and Control*, 29(1), 1-13.

Jian Huang, Zhi-Hong Guan, Matsuno, T., Fukuda, T., & Sekiyama, K. (2010). Sliding-mode velocity control of mobile-wheeled inverted-pendulum systems. *IEEE Transactions on Robotics*, 26(4), 750-758.

Johnson, T., Zhou, S., Cheah, W., Mansell, W., Young, R., & Watson, S. (2020). Implementation of a perceptual controller for an inverted pendulum robot. *Journal of Intelligent & Robotic Systems*, 99(3), 683-692.

Kim, Y., Kim, S. H., & Kwak, Y. K. (2006). Dynamic analysis of a nonholonomic two-wheeled inverted pendulum robot. *Journal of Intelligent & Robotic Systems*, 44(1), 25-46.

Maity, S., & Luecke, G. R. (2019). Stabilization and Optimization of Design Parameters for Control of Inverted Pendulum. *Journal of Dynamic Systems, Measurement, and Control*, 141(8).

Maxongroup (2012). https://www.maxongroup.com/maxon/view/news/MEDIENMITTEILUNG-EC60-flat-MILE-EN https://www.maxongroup.co.uk/medias/sys_master/root/8841185656862/EN-294.pdf

McCaffrey, D., & Banks, S. P. (2001). Lagrangian manifolds and asymptotically optimal stabilizing feedback control. *Systems & control letters*, *43*(3), pp. 219-224.

McGeer, T. (1990). Passive dynamic walking. The *International Journal of Robotics Research*, 9(2), 62-82.

Nadda, S., & Swarup, A. (2020). A novel sliding mode composite control design for fast time performance of quadrotor UAV. *International Journal of Modelling, Identification and Control*, 34(1), 26-32.

Ogata, K. (2002). Modern Control Engineering, *Prentice Hall*, fourth edition.

Pathak, K., Franch, J., & Agrawal, S. K. (2005). Velocity and position control of a wheeled inverted pendulum by partial feedback linearization. *IEEE Transactions on Robotics*, 21(3), 505-513.

Ren, T., Chen, T., & Chen, C. (2008). Motion control for a two-wheeled vehicle using a self-tuning PID controller. *Control Engineering Practice*, 16(3), 365-375.

Rigatos, G., Busawon, K., Pomares, J., & Abbaszadeh, M. (2020). Nonlinear optimal control for the wheeled inverted pendulum system. *Robotica*, *38*(1), pp. 29-47.

Salerno, A., & Angeles, J. (2003). On the nonlinear controllability of a quasiholonomic mobile robot. 2003 *IEEE International Conference on Robotics and Automation*, 3, 3379–3384 vol.3.

Segway Inc. (2020). Segway i2 SE. Retrieved from https://uk-en.segway.com/products/segway-i2-se

Shalaby, R., El-Hossainy, M., & Abo-Zalam, B. (2019). Fractional order modeling and control for under-actuated inverted pendulum. *Communications in Nonlinear Science and Numerical Simulation*, 74, 97-121.

Spong, M. W. (1995). The swing up control problem for the acrobot. *IEEE Control Systems*, 15(1), 49-55.

Spong, M. W., & Block, D. J. (1995). The Pendubot: a mechatronic system for control research and education. *Proceedings of 1995 34th IEEE Conference on Decision and Control*, 1, 555–556 vol.1.

Xu, X., Zhang, H., & Carbone, G. (2017). Case studies on nonlinear control theory of the inverted pendulum. Boubaker, O., & Iriarte, R. (Eds.). *The Inverted Pendulum in Control Theory and Robotics: From Theory to New Innovations*, Vol. *111*, pp. 225, IET.

Yamamoto, Y. (2009). NXTway-GS (Self-Balancing Two-Wheeled Robot) Controller Design (https://www.mathworks.com/matlabcentral/fileexchange/19147-nxtway-gs-self-balancing-two-wheeled-robot-controller-design), *MATLAB Central File Exchange*. Retrieved August 7, 2020.